Article ID: 1000-324X(2018)09-1022-07 **DOI:** 10.15541/jim20180143

Facile Synthesis of Reduced Graphene Oxide *In-situ* Wrapped $MnTiO_3$ Nanoparticles for Excellent Lithium Storage

LIU Huan-Long[1,2], ZHAO Wei[2], LI Rui-Zhe[2], HUANG Xie-Yi[2],
TANG Yu-Feng[2], LI Dong-Mei[1], HUANG Fu-Qiang[2,3]

(1. School of Material Science and Engineering, Shanghai University, Shanghai 200444, China; 2. State Key Laboratory of High Performance Ceramics and Superfine Microstructure, Shanghai Institute of Ceramics, Chinese Academy of Sciences, Shanghai 200050, China; 3. Beijing National Laboratory for Molecular Sciences and State Key Laboratory of Rare Earth Materials Chemistry and Applications, College of Chemistry and Molecular Engineering, Peking University, Beijing 100871, China)

Abstract: The stable high-capacity anode has been an urgent demand for high energy density lithium-ion batteries (LIBs). Herein, a simple and effective strategy to synthesize high-performance reduced graphene oxide (rGO) *in-situ* wrapped $MnTiO_3$ nanoparticles ($MnTiO_3$@rGO) by Sol-Gel method is designed. The $MnTiO_3$ nanoparticles are uniformly dispersed and wrapped by few-layer graphene. Due to high conductivity of rGO, $MnTiO_3$@rGO nanoparticles show excellent rate performance, with a specific capacity of 286 $mAh\cdot g^{-1}$ being displayed at the higher rate of 5.0 $A\cdot g^{-1}$. Moreover, benefited from porous structure and flexible rGO shell, the $MnTiO_3$@rGO anode delivers a remarkable long-term cycling stability. The specific capacity maintains 441 $mAh\cdot g^{-1}$ after 500 cycles at 0.5 $A\cdot g^{-1}$, only losing 8.4%. Therefore, the results demonstrate that the facile synthetic strategy is highly desirable for improving the conductivity and stability of metal oxide anodes.

Key words: *in-situ* wrapped; reduced oxide graphene; $MnTiO_3$ nanoparticles; lithium-ion batteries anode

The transition metal oxides (MnO[1], Fe_2O_3[2-3], CoO[4], NiO[5], *etc*.) have been considered as promising anode materials for lithium-ion batteries (LIBs) due to their high theoretical capacity (~800 $mAh\cdot g^{-1}$), wide availability, and low cost[6-8]. However, the terrible cycle stability and poor rate capability of conversion-type anode is still impeding practical applications[9]. Above mentioned problems are mainly due to the conversion-type transition metal oxides anode undergoing a large volume expansion with lithium ions insertion/extraction, rapid capacity degradation[10]. The stable electrochemical performance of the electrode material is mainly related to the structure design and conductivity of the material. To obtain the excellent electrode material, many strategies have been applied to synthesize electrode materials with effectively reserved expansion space and improved electric conductivity, including the design of the unique hierarchical nanostructures materials (such as hollow[11], core-shell[12], yolk-shell structure[13] and various morphology, *etc*.) and composite materials[14-16]. In terms of composite materials, carbonaceous materials, such as activated carbon[17-18], carbon nanotubes[19]and graphene[20], *etc*., have been widely developed as coating shell or conductive additives. The carbon materials could buffer the volume change and enhance the electric transmission of electrode materials during the charging/discharging process[21].

Unfortunately, although the scale synthesis electrode of "A+B" mode electrode could improve the electrochemical performance, the effects were far from satisfactory[22]. The weak interfacial adhesion between carbon shell and transition metal oxides electrode could not effectively protect the integrity of the material structure, leading to the relative low capacity[23-26]. In addition, the *in-situ* growing graphene shell on the transition metal oxides surface is an interesting designing idea, including chemical vapor deposition (CVD) or plasma methods. The growing conductivity graphene has an excellent electric transmission and flexible mechanical nature, accommodating the volume expansion and providing excel-

Received date: 2018-04-03; **Modified date:** 2018-05-11
Foundation item: National Key Research and Development Program (2016YFB0901600); Science and Technology Commission of Shanghai (16ZR1440500, 16JC1401700); National Science Foundation of China (51672301); Key Research Program of Chinese Academy of Sciences (QYZDJ-SSW-JSC013, KGZD-EW-T06); Youth Innovation Promotion Association CAS
Biography: LIU Huan-Long (1990–), male, candidate of Master degree. E-mail: huanlongliu@outlook.com
Corresponding author: HUANG Fu-Qiang, professor. E-mail: huangfq@mail.sic.ac.cn; LI Dong-Mei, associate professor. E-mail: dmli@mail. shu.edu.cn

lent conductivity layer during charging/discharging[27]. However, the *in-situ* growing graphene is expensive and difficult to control, meanwhile this method requires the catalyst in electrode materials, such as Fe, Ni, and Cu, *etc*[28]. So, it is difficult to have a low-cost and facile process for graphene coating transition metal oxides electrodes.

According to the previous reported works[20,27], the combination of TiO_2 and transition metal oxide can hinder the aggregation of metal particles and accommodate the volumetric expansion of the electrode material, improving the electrochemical performance. Thus, the $MnTiO_3$ becomes a promising anode material for LIBs by improving the electrochemical performances with the introduction of TiO_2. Although the poor conductivity of $MnTiO_3$ is still a hindrance to maintain excellent performance, carbon coating shell is an effective strategy to improve the conductivity and enhance the stability of semiconductor $MnTiO_3$ with cycling. Herein, a facile strategy to synthesize the reduced graphene oxide *in-situ* wrapped $MnTiO_3$ nanoparticles ($MnTiO_3$@rGO) by the Sol−Gel method was designed. The perfectly encapsulated few-layer rGO shell provides fast pathway for electron transportation, improving the lithium dynamics. The few-layer rGO with excellent mechanical nature refrains the aggregation of $MnTiO_3$ nanoparticles and suppresses fracture of particles and electrode stress during lithiation/delithiation[29]. In addition, the solid electrolyte interface (SEI) film could grow uniformly on the graphene surface, preventing the side reactions occurrence of electrode. All the features induced by *in-situ* wrapped rGO resulted in excellent and stable electrochemical performances for $MnTiO_3$@rGO[30].

1 Experimental

1.1 Preparation of $MnTiO_3$ nanoparticles

The tetrabutyl titanate (TBT) and manganese titanate were purchased from Alladin, and ethylene glycol (EG) was purchased from Sinopharm Chemical Reagent Co., Ltd. The typical synthetic procedure for $MnTiO_3$@rGO nanoparticles composites is described as follows. 150 mL EG and 120 mg GO were added into a three-mouth flask with ultrasonic stirring, and nitrogen was used as inert gas. 3.4 mL TBT and 2.45 g manganese acetate were dissolved under vigorous stirring to form a red solution, and kept stirring overnight. Ultimately, the resultant precipitate was collected by centrifugation. The precipitate was annealed at 1073 K for 2 h in Ar atmosphere, obtaining a black powder of mesoporous $MnTiO_3$@rGO nanoparticles. The $MnTiO_3$ nanoparticles were obtained following the same procedure without GO.

1.2 Characterization of Samples

Samples measurements: the crystalline structure and morphology of the samples were characterized by X-ray diffraction measurement (XRD, Bruker D8 ADVANCE, CuKa radiation), and transmission electron microscopy (TEM, JEM 2100F), respectively. Nitrogen adsorption/desorption isotherms were measured using a Micrometitics Tristar 3000 system. The pore-size distributions were calculated from desorption branches of isotherms by the Barrett–Joyner–Halenda (BJH) method.

1.3 Electrochemical testing

The electrochemical performances of the as-obtained samples were evaluated by a 2016-type coin cell. The working electrode was composed of 80wt% of active material, 10wt% of conductivity agent (acetylene black), and 10wt% of binder (PVDF, Aldrich) solvating onto the Cu foil and then dried at 343 K overnight. The cells were assembled in an argon-filled glove box (moisture and oxygen contents below 0.1×10^{-6}) by using the electrode as the working electrode, lithium metal as the counter electrode, Celgard 2600 as separator, and 1 mol/L $LiPF_6$ (dissolved in ethylene carbonate and dimethyl carbonate with a 1∶1 volume ratio) as the electrolyte. The galvanostatic discharge/charge tests were performed in the CT2001A battery testing system (Land®, China) at 298 K with a voltage window of 0.01 V–3.0 V. The cyclic voltammetry (CV) and EIS tests were conducted on a CHI electrochemical workstation.

2 Results and discussion

The $MnTiO_3$@rGO nanoparticles were synthesized by reacting tetraethyl titanate with manganese acetate in the graphene oxide (GO) solution, followed by calcination in Ar atmosphere. From the SEM image (Fig. 1(a)), the surface of mesoporous $MnTiO_3$@rGO nanoparticles are closely bound together with graphene shell. The optical photograph of $MnTiO_3$@rGO powder is exhibited, emphasizing the capacity of scale preparation. A uniform size of ~15 nm of mesoporous $MnTiO_3$@rGO nanoparticles confirmed by the TEM images (Fig. 1(b)). As shown in the high-resolution TEM (HRTEM) image (Fig. 1(c)), the lattice spacing of the $MnTiO_3$ nanoparticle is measured to be ~0.28 nm, which agrees well with the *d*-spacing of the pyrophanite $MnTiO_3$ (104) plane. The $MnTiO_3$@rGO nanoparticle with a perfectly wrapped graphene shell around the highly crystalline core structure can be clearly observed. The *in-situ* wrapped rGO shell reveals a few-layer structure of about 2–4 layers graphene. As shown in the Fig. 1(d), the selected-area electron diffraction (SAED) pattern of $MnTiO_3$@rGO displayed the ring-like mode, indicating polycrystalline

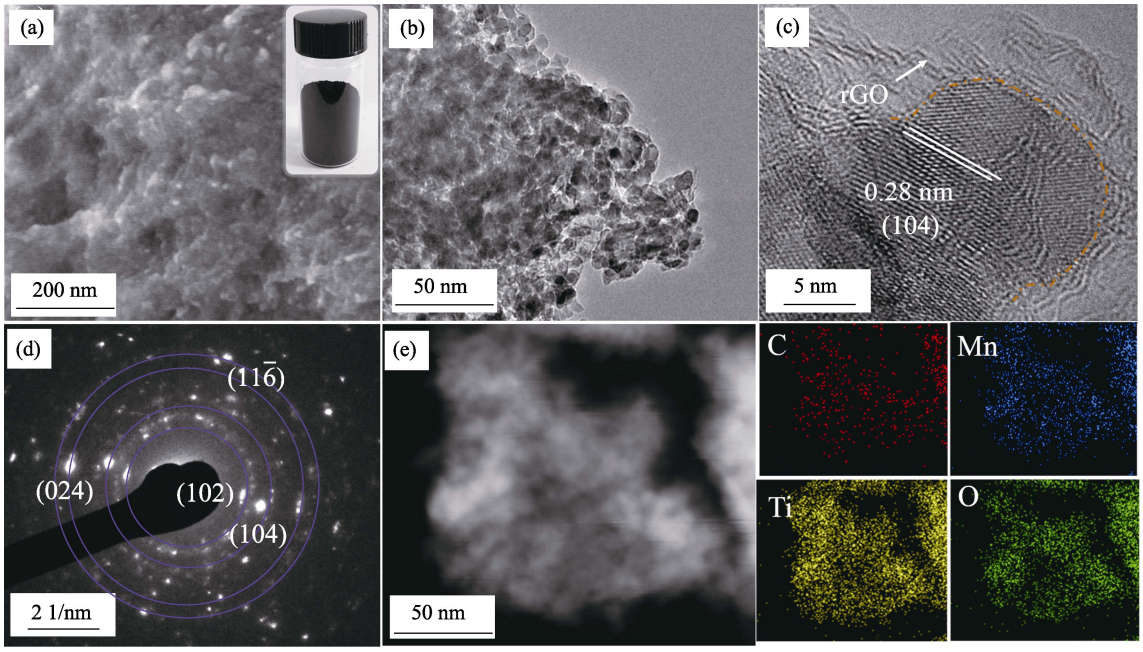

Fig. 1 (a) SEM image with inset showing the optical photograph of $MnTiO_3$@rGO powder, (b) TEM image, (c) HRTEM image, and (d) SAED pattern, (e) high-angle annular dark field (HAADF) of $MnTiO_3$@rGO, and EDS mapping of C, Mn, Ti, and O elements which indicates uniformly elemental distribution in the $MnTiO_3$@rGO

structure. The ring-like pattern can be clearly assigned to the diffractions of the (012), (104), (024), and (11$\bar{6}$) planes, respectively, which is consistent with the aforementioned XRD results. The high-angle annular dark field (HAADF) of $MnTiO_3$@rGO was investigated by scanning transmission electron microscopy (STEM) (Fig. 1(e)). The energy dispersed spectrum (EDS) of $MnTiO_3$@rGO shows the existence of C, Mn, Ti, and O elements and respective contents (Table 1). Corresponding elemental mapping results indicate the homogeneous distribution of C, Mn, Ti, and O elements.

To further investigate the intrinsic structure of as-obtained samples, the X-ray diffraction (XRD) pattern of the samples are presented in Fig. 2(a). The characteristic diffraction peaks within the 2θ range from 20° to 80° could be well indexed to the (012), (104), (110), (11$\bar{3}$), (024), (11$\bar{6}$), (018), (12$\bar{4}$), and (300) planes for pyrophanite $MnTiO_3$ (JCPDS No.77-1858). The (002) diffraction peak of graphene exists at 26.5° indicating the GO fully reduced to rGO *via* the high temperature procedure. In addition, the characteristic peaks of other impurities such as MnO, and TiO_2 do not appear, indicating the pure $MnTiO_3$ phase.

The Raman spectra (Fig. 2(b)) demonstrated the existence of rGO and $MnTiO_3$ in $MnTiO_3$@rGO composites. Compared with $MnTiO_3$, the stronger Raman peaks locating at 1340 cm^{-1} and 1591 cm^{-1} for $MnTiO_3$@rGO are typical D and G bands, respectively, inducing the existence of rGO, which is consistent with the HRTEM result. The existence of D and G bands for $MnTiO_3$ could be ascribed to glycol carbonized in the precursors during annealing. The presence of typical Raman-active modes of $MnTiO_3$ is located at 153 cm^{-1}, 202 cm^{-1}, 232 cm^{-1}, 284 cm^{-1}, 338 cm^{-1}, 389 cm^{-1}, 458 cm^{-1}, 608 cm^{-1}, 705 cm^{-1}, and 760 cm^{-1}. The strong Raman absorption peak of $MnTiO_3$ nanoparticles locates at 682 cm^{-1}, which is due to the high-frequency vibration mode of MnO_6 octahedron. The phonon mode absorption peaks below 300 cm^{-1} are caused by the lattice vibration. These results coincide with XRD pattern and TEM observation.

Table 1 EDS data of $MnTiO_3$@rGO

Materials	C/wt%	O/wt%	Ti/wt%	Mn/wt%
$MnTiO_3$@rGO	9.01	18.87	32.11	40.01

Nitrogen sorption isotherms of the mesoporous $MnTiO_3$@rGO showed a type-IV curve (Fig. 2(c)). The specific surface area is calculated to be 91 $m^2 \cdot g^{-1}$, which is higher than that of $MnTiO_3$ (12 $m^2 \cdot g^{-1}$). The corresponding pore size distribution of $MnTiO_3$@rGO are mainly within 3 nm due to the accumulation of nanoparticles. The porous structure could reserve more space to accommodate the volume expansion of the electrode and improve lithium ions transportation during charging/discharging. In addition, the conductivity of $MnTiO_3$ and $MnTiO_3$@rGO is investigated by the two electrode methods, the results indicate that the electrical conductivity of the $MnTiO_3$@rGO sample reaches 2.37 $mS \cdot cm^{-1}$, which is higher than that of $MnTiO_3$ due to the conductive rGO coating shell (Fig. 2(d)). These are beneficial for excellent electrochemical performance of $MnTiO_3$@rGO anode.

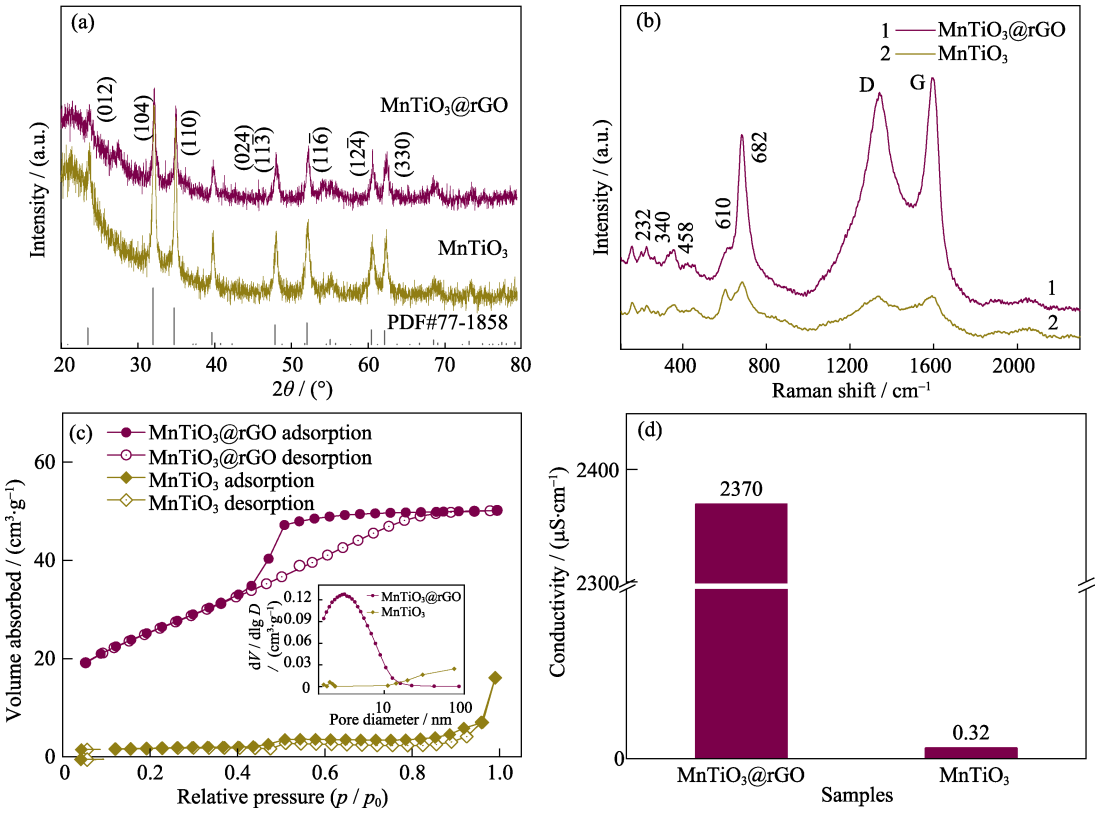

Fig. 2　(a) XRD patterns, (b) Raman spectra in the range of 100–2000 cm^{-1}, (c) nitrogen sorption isotherms and corresponding pore size distribution curves (inset), and (d) electrical conductivity of as-obtained materials

To evaluate the electrochemical performance of $MnTiO_3$@rGO electrode, cyclic voltammetry (CV) and galvanostatic cycling were carried out by assembling half-cells with lithium metal foils as counter and reference electrodes. All of the electrode mass consist of $MnTiO_3$ and rGO in the $MnTiO_3$@rGO electrode. The type of electrochemical reactions are probed by initial three CV with a voltage window of 0.01–3.0 V. The CV curves at a sweep rate of 0.2 $mV·s^{-1}$ was shown in Fig. 3(a). In the first discharge process, the cathodic peak located around 0.72 V correlates with the formation of solid electrolyte interface (SEI) film and the others at 1.71 V and 0.38 V, indicating the lithium ions insertion into TiO_2 and the reduction of MnO to metal Mn[1, 31]. In the subsequent charge process, two broad anodic peaks occurring around 1.25 V and 1.75 V are correspond to the oxidation of Mn to Mn^{2+} and lithium ions extraction from TiO_2, respectively[32]. From the second cycle, there is only a broadened reduction peak in the range of 0.3 V–0.5 V due to the overlap and broadening of peaks[33-34].

Besides, the CV curves of the second and third cycles tend to overlap, demonstrating the excellent cycling performance. In Fig. 3(b), the rate capability of the $MnTiO_3$@rGO was investigated by increasing the current densities from 0.1 $A·g^{-1}$ to 5.0 $A·g^{-1}$. Compared with $MnTiO_3$, the rate performance of $MnTiO_3$@rGO electrode significantly outperformed that of $MnTiO_3$ anode. The corresponding charge/discharge curves are shown in Fig. 4(a). The $MnTiO_3$@rGO electrode performed excellently under high current densities of 2.0 $A·g^{-1}$, and 5.0 $A·g^{-1}$, with the specific capacity recorded as 342 $mAh·g^{-1}$and 286 $mAh·g^{-1}$, respectively.

To demonstrate excellent cycle stability, long cycle performance of as-obtained materials was compared[35]. Fig. 3(c) reveals the cycle stability and coulombic efficiency of $MnTiO_3$@rGO and $MnTiO_3$ electrode. Serious capacity attenuation with cycling occurs on the $MnTiO_3$ electrode. The poor conductivity of $MnTiO_3$ causes a considerable lithium kinetic obstacle for lithium ions extraction and particles are pulverized, which induces irreversible capacity. In addition, the rGO electrode shows the excellent cycling stability. This greatly improves the cycling stability of $MnTiO_3$@rGO. During the cycle testing, the coulombic efficiency of $MnTiO_3$@rGO is above 98.8%, and the specific capacity is maintained 441 $mAh·g^{-1}$ after 500 cycles, losing 8.4% referring to the initial capacity at a current density of 0.5 $A·g^{-1}$.

The excellent electrochemical performance mainly stems from the synergistic effect between the $MnTiO_3$ nanostructures and *in-situ* wrapped few-layer rGO shell. The porous $MnTiO_3$@rGO has a greater specific surface area than that of $MnTiO_3$, decreasing the transport

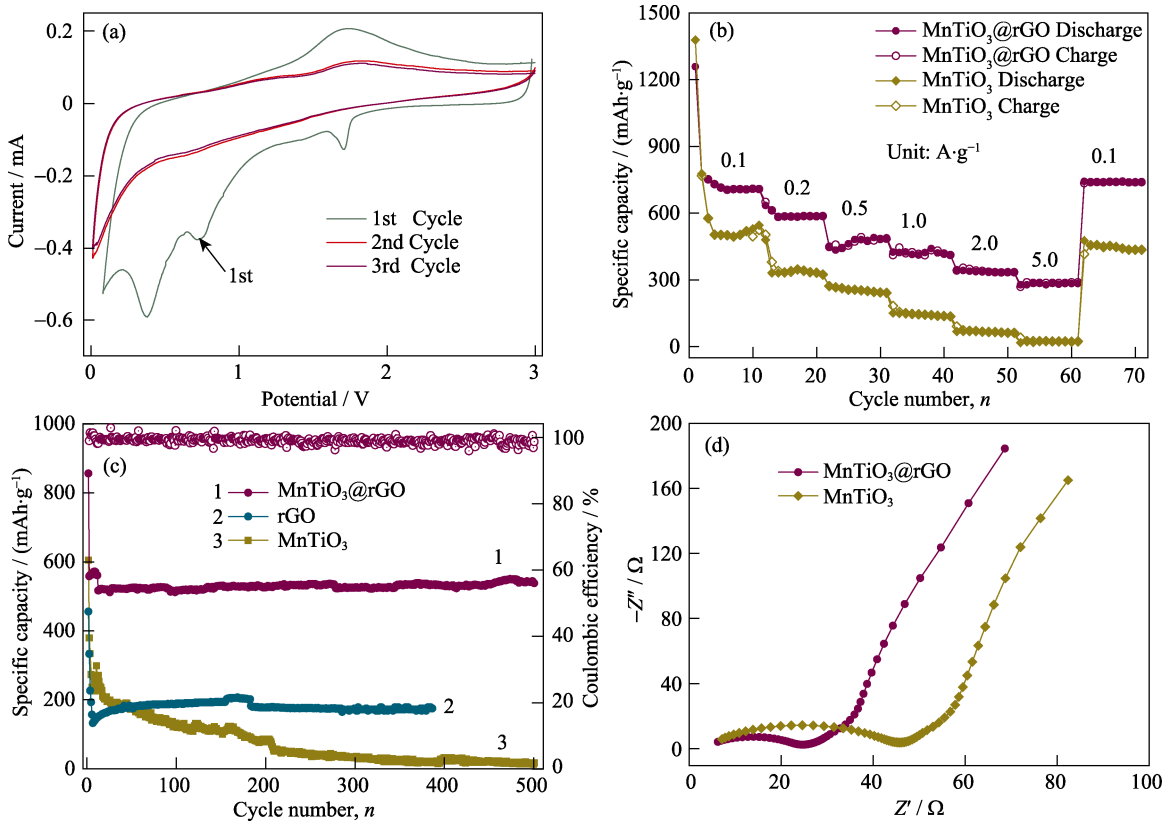

Fig. 3 Electrochemical measurements of samples

(a) CV curves of $MnTiO_3$@rGO electrode; (b) Comparison of the specific capacity at different rates; (c) Cycling performance at 0.5 $A·g^{-1}$ between $MnTiO_3$@rGO, rGO and $MnTiO_3$ electrodes; (d) Nyquist plots of electrodes of $MnTiO_3$@rGO and $MnTiO_3$ after 3 cycling. All of the measurements were conducted using a voltage window of 0.01 V–3.0 V

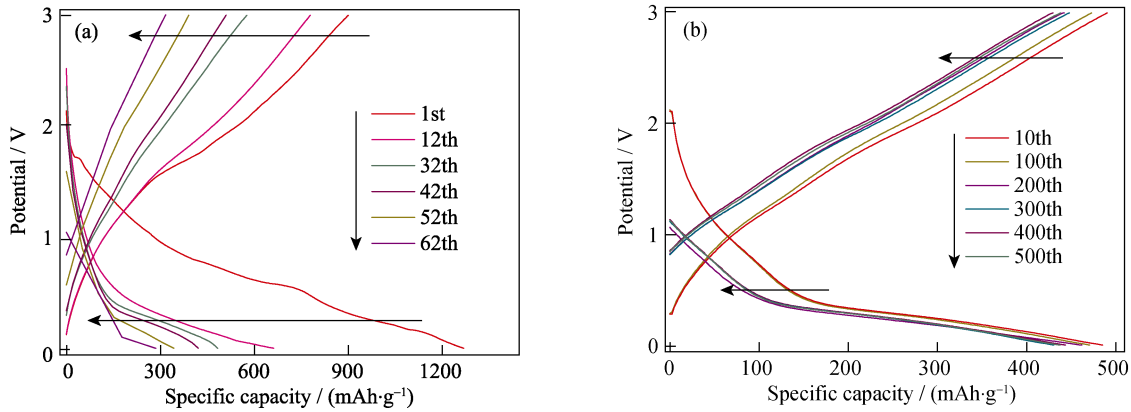

Fig. 4 (a) Capacity retention curves *versus* various current densities, and (b) capacity retention curves *versus* various cycles of $MnTiO_3$@rGO anodes

distance of lithium ions of electrochemical reactions. In addition, the rGO shell not only inhibits the aggregation of the $MnTiO_3$ nanoparticles, enhancing the lithium kinetics, but also helps the forming of a stable SEI film, avoiding the electrolyte decomposition. As shown in Fig. 4(b), the galvanostatic charge/discharge profiles of the $MnTiO_3$@rGO electrode with cycle numbers of 10th, 100th, 200th, 300th, 400th, and 500th were demonstrated. The low discharge platform is consistent with the CV results. Fig. 3(d) compares the Nyquist plots of electrodes of $MnTiO_3$@rGO and $MnTiO_3$ after three cycling. The semicircle at high-medium frequency and the straight line at low frequency are displayed, corresponding to charge transfer and diffusion, respectively. Apparently, the $MnTiO_3$@rGO electrode shows a much lower resistance than the $MnTiO_3$ electrode (24 *vs*. 46 Ω). These largely ascribe to the highly conductive rGO shell, facilitating electron transfer from $MnTiO_3$ within the

whole electrode and thus decrease resistance.

3 Conclusion

In summary, a general and scale strategy was designed for *in-situ* wrapped of conductive few-layer rGO shell on $MnTiO_3$ materials *via* a facile Sol-Gel method. After the high temperature annealing, $MnTiO_3$ nanoparticles are tightly encapsulated with few-layers rGO. Benefiting from the conductive rGO and $MnTiO_3$ nanoparticles, the $MnTiO_3$@rGO electrode revealed the excellent rate performance that the specific capacity of 342 $mAh \cdot g^{-1}$ and 286 $mAh \cdot g^{-1}$ were performed under high current densities of 2.0 $A \cdot g^{-1}$, and 5.0 $A \cdot g^{-1}$. In addition, the porous structure and flexible rGO could accommodate the large volume change, maintaining the electrode stability during lithiation/delithiation. The resultant $MnTiO_3$@rGO nanocomposite exhibited a reversible capacity of 484 $mAh \cdot g^{-1}$at 0.5 $A \cdot g^{-1}$ after 500 cycles (only losing 8.4%). Interestingly, the facile and effective preparation method could be extended to synthesize high stability nano-structure metal oxide anode for LIBs.

References:

[1] KANG D, LIU Q, SI R, *et al*. Crosslinking-derived MnO/carbon hybrid with ultrasmall nanoparticles for increasing lithium storage capacity during cycling. *Carbon*, 2016, **99:** 138–147.

[2] JIANG Y, ZHANG D, LI Y, *et al*. Amorphous Fe_2O_3 as a high-capacity, high-rate and long-life anode material for lithium ion batteries. *Nano Energy*, 2014, **4:** 23–30.

[3] PETNIKOTA S, MARKA S K, BANERJEE A, *et al*. Graphenothermal reduction synthesis of 'exfoliated graphene oxide/iron (II) oxide' composite for anode application in lithium ion batteries. *Journal of Power Sources*, 2015, **293:** 253–263.

[4] DO J S, WENG C H. Preparation and characterization of CoO used as anodic material of lithium battery. *Journal of Power Sources*, 2005, **146(1):** 482–486.

[5] VARGHESE B, REDDY M V, YANWU Z, *et al*. Fabrication of NiO nanowall electrodes for high performance lithium ion battery. *Chemistry of Materials*, 2008, **20(10):** 3360–3367.

[6] LI B, HAO W, WEN X G. Semi-hollow/solid $ZnMn_2O_4$ microspheres: synthesis and performance in Li ion battery. *Journal of Inorganic Materials*, 2018, **33(3):** 307–312.

[7] CAI J X, LI Z P, LI W, *et al*. Synthesis and electrochemical performance of Fe_2O_3 nanofibers as anode materials for LIBs. *Journal of Inorganic Materials*, 2018, **33(3):** 301–306.

[8] LIU S Y, XU L, CHEN X, *et al*. Cluster structural $CoFe_2O_4$ particles loaded onto graphene and its Li-storage performance. *Journal of Inorganic Materials*, 2017, **32(9):** 904–908.

[9] GUO Y G, HU J S, WAN L J. Nanostructured materials for electrochemical energy conversion and storage devices. *Advanced Materials*, 2008, **20(15):** 2878–2887.

[10] KIM A, PARK E, LEE H, *et al*. Highly reversible insertion of lithium into MoO_2 as an anode material for lithium ion battery. *Journal of Alloys and Compounds*, 2016, **681:** 301–306.

[11] YAO Y, MCDOWELL M T, RYU I, *et al*. Interconnected silicon hollow nanospheres for lithium-ion battery anodes with long cycle life. *Nano Letters*, 2011, **11(7):** 2949–2954.

[12] CUI L F, RUFFO R, CH C K, *et al*. Crystalline-amorphous core−shell silicon nanowires for high capacity and high current battery electrodes. *Nano Letters*, 2009, **9(1):** 491–495.

[13] GUAN C, SUMBOJA A, WU H, *et al*. Hollow Co_3O_4 nanosphere embedded in carbon arrays for stable and flexible solid-state zinc–air batteries. *Advanced Materials*, 2017, **29(44):** 1704117–1–9.

[14] HASSOUN J, DERRIEN G, PANERO S, *et al*. A nanostructured Sn–C composite lithium battery electrode with unique stability and high electrochemical performance. *Advanced Materials*, 2008, **20(16):** 3169–3175.

[15] LIAO L X, WANG M, FANG T, *et al*. Synthesis and characterization of $ZnFe_2O_4$ anode for lithium ion battery. *Journal of Inorganic Materials*, 2016, **31(1):** 34–38.

[16] WANG Y P, LIU J J, LIU C X, *et al*. Morphology-controlled synthesis of hollow core-shell structural alpha-MoO_3-SnO_2 with superior lithium storage. *Journal of Inorganic Materials*, 2015, **30(9):** 919–924.

[17] WANG Y G, CHENG L, XIA Y Y. Electrochemical profile of nano-particle CoAl double hydroxide/active carbon supercapacitor using KOH electrolyte solution. *Journal of Power Sources*, 2006, **153(1):** 191–196.

[18] HAO Y, QIAN M, XU J, *et al*. Porous cotton-derived carbon: synthesis, microstructure and supercapacitive performance. *Journal of Inorganic Materials*, 2018, **33(1):** 93–99.

[19] WANG B, XIN H, LI X, *et al*. Mesoporous CNT@TiO_2-C nanocable with extremely durable high rate capability for lithium-ion battery anodes. *Scientific Reports*, 2014, **4:** 3729.

[20] XU J, DONG W, SONG C, *et al*. Black rutile (Sn, Ti)O_2 initializing electrochemically reversible Sn nanodots embedded in amorphous lithiated titania matrix for efficient lithium storage. *Journal of Materials Chemistry A*, 2016, **4(40):** 15698–15704.

[21] TAN X, CUI C, WU S, *et al*. Nitrogen-doped mesoporous carbon-encapsulated MoO_2 nanobelts as a high-capacity and stable host for lithium-ion storage. *Chemistry, an Asian Journal*, 2017, **12(1):** 36–40.

[22] HOLZAPFEL M, BUQA H, SCHEIFELE W, *et al*. A new type of nano-sized silicon/carbon composite electrode for reversible lithium insertion. *Chemical Communications*, 2005**(12):** 1566–1568.

[23] LI J, ZHANG L, ZHANG L, *et al*. *In-situ* growth of graphene decorations for high-performance $LiFePO_4$ cathode through solid-state reaction. *Journal of Power Sources*, 2014, **249:** 311– 319.

[24] LI W, ZHANG Y J, WANG X P, *et al*. Synthesis and electrochemical performance of $LiMn_{0.6}Fe_{0.4}PO_4$/C cathode for lithium-ion batteries. *Journal of Inorganic Materials*, 2017, **32(5):** 476–482.

[25] YANG T, LI X, TIAN X D, *et al*. Preparation and electrochemical performance of Si@C/SiO_x as anode material for lithium-ion batteries. *Journal of Inorganic Materials*, 2017, **32(7):** 699–704.

[26] LIANG P, XING S, SHU H B, *et al*. Analogous three-dimensional MoS_2/graphene composites for reversible Li storage. *Journal of Inorganic Materials*, 2016, **31(6):** 575–580.

[27] XU J, DING W, ZHAO W, *et al*. *In situ* growth enabling ideal graphene encapsulation upon mesocrystalline $MTiO_3$ (M = Ni, Co, Fe) nanorods for stable lithium storage. *ACS Energy Letters*, 2017, **2(3):** 659–663.

[28] GEIM A, KNOVOSELOV K S. The rise of graphene. *Nature Materials*, 2007, **6:** 183–191.

[29] EDA G, FANCHINI G, CHHOWALLA M. Large-area ultrathin films of reduced graphene oxide as a transparent and flexible electronic material. *Nature Nanotechnology*, 2008, **3:** 270–274.

[30] ZHU X, ZHU Y, MURALI S, *et al*. Nanostructured reduced graphene

oxide/Fe_2O_3 composite as a high-performance anode material for lithium ion batteries. *ACS Nano*, 2011, **5(4):** 3333–3338.

[31] YUAN T, JIANG Y, SUN W, *et al*. Ever-increasing pseudocapacitance in RGO–MnO–RGO sandwich nanostructures for ultrahigh-rate lithium storage. *Advanced Functional Materials*, 2016, **26(13):** 2198–2206.

[32] BAI X, LI T, ZHAO X Y, *et al*. Al_2O_3-modified Ti-Mn-O nanocomposite coated with nitrogen-doped carbon as anode material for high power lithium-ion battery. *RSC Advances*, 2016, **6(47):** 40953–40961.

[33] GUO S, LIU J, QIU S, *et al*. Porous ternary TiO_2/$MnTiO_3$@C hybrid microspheres as anode materials with enhanced electrochemical performances. *Journal of Materials Chemistry A*, 2015, **3(47):** 23895–23904.

[34] YANG L, ZHANG X, LI Y, *et al*. Graphene-encapsulated $Li_2MnTi_3O_8$ nanoparticles as a high rate anode material for lithium-ion batteries. *Electrochimica Acta*, 2015, **155:** 272–278.

[35] LIU Z, TANG Y F, LIN T Q, *et al*. Preparation and characterization of graphene-MoS_2 composite anode materials. *Journal of Inorganic Materials*, 2016, **31(4):** 345–350.

还原氧化石墨烯原位包覆纳米 $MnTiO_3$ 颗粒的简易合成及储锂性能研究

刘焕龙[1,2], 赵 伟[2], 李睿哲[2], 黄谢意[2], 唐宇峰[2], 李冬梅[1], 黄富强[2,3]

(1. 上海大学 材料科学与工程学院, 上海 200444; 2.中国科学院 上海硅酸盐研究所, 高性能陶瓷和超微结构国家重点实验室, 上海 200050; 3. 北京大学 化学与分子工程学院, 北京分子科学国家实验室, 稀土材料化学及应用国家重点实验室, 北京 100871)

摘 要: 对于高能量密度的锂离子电池而言, 研究稳定、高容量负极材料的需求十分迫切。基于此, 本工作设计了一种简单有效的溶胶–凝胶法, 来合成高性能的被还原石墨烯氧化物原位包覆的 $MnTiO_3$ 纳米颗粒($MnTiO_3$@rGO)。合成的 $MnTiO_3$ 纳米粒子分散均匀, 被少层的石墨烯包裹。由于还原氧化石墨烯的高电导率, $MnTiO_3$@rGO 作为锂离子电池负极表现出优异的倍率性能, 在 5.0 $A\cdot g^{-1}$ 的高电流密度时, $MnTiO_3$@rGO 展现出了 286 $mAh\cdot g^{-1}$ 的比容量。此外, 得益于 $MnTiO_3$@rGO 的多孔结构和柔性的还原氧化石墨烯外层, $MnTiO_3$@rGO 负极具有显著的长期循环稳定性。在 500 个循环后, 比容量仍保持在 441 $mAh\cdot g^{-1}$, 仅损失了 8.4%。结果表明, 该方法对提高金属氧化物负极的导电性和循环稳定性具有较高的应用价值。

关 键 词: 原位包覆; 还原氧化石墨烯; $MnTiO_3$ 纳米颗粒; 锂离子电池负极

中图分类号: TQ174 **文献标识码:** A